Experimental and Theoretical Investigation of the Anti-Ferromagnetic Coupling of Cr(III) Ions through Diamagnetic -O-Nb(V)-O- Bridges

Marijana Jurić, Lidija Androš Dubraja, Damir Pajić, Filip Torić, Andrej Zorko, Andrew Ozarowski, Vito Despoja, William Lafargue-Dit-Hauret, Xavier Rocquefelte

Experimental and Theoretical Investigation of the Antiferromagnetic Coupling of Cr^{III} Ions through Diamagnetic –O–Nb^{V}–O– Bridges

Marijana Jurić,[a,] Lidija Androš Dubraja,[a] Damir Pajić,[b,]* Filip Torić,[b] Andrej Zorko,[c]*

Andrew Ozarowski,[d] Vito Despoja,[b] William Lafargue-Dit-Hauret,[e] and Xavier Rocquefelte[e]

[a]Ruđer Bošković Institute, Bijenička cesta 54, 10000 Zagreb, Croatia

[b]Department of Physics, Faculty of Science, University of Zagreb, Bijenička cesta 32, 10000 Zagreb, Croatia

[c]Jožef Stefan Institute, Jamova cesta 39, 1000 Ljubljana, Slovenia

[d]National High Magnetic Field Laboratory, Florida State University, Tallahassee, Florida 32310, USA

[e]Institut des Sciences Chimiques de Rennes, UMR 6226 CNRS, Université de Rennes 1, Rennes, France

Marijana.Juric@irb.hr, Lidija.Andros@irb.hr, dpajic@phy.hr, ftoric@phy.hr, andrej.zorko@ijs.si, ozarowsk@magnet.fsu.edu, vito@phy.hr, william.lafargue-dit-hauret@univ-rennes1.fr, xavier.rocquefelte@univ-rennes1.fr

Dr. Marijana Jurić

Ruđer Bošković Institute

Bijenička cesta 54

10000 Zagreb, Croatia

Tel.: +385 1 4561189

Fax: +385 1 4680098

E-mail: Marijana.Juric@irb.hr

Dr. Damir Pajić

Department of Physics

Faculty of Science, University of Zagreb

Bijenička cesta 32

10000 Zagreb, Croatia

Tel: +385 1 4605538

Fax: +385 1 4680336

E-mail: dpajic@phy.hr

ABSTRACT. The synthesis and properties of a novel heterotetranuclear compound $[Cr_2(bpy)_4(\mu\text{-}O)_4Nb_2(C_2O_4)_4]\cdot 3H_2O$ (**1**; bpy = 2,2'-bipyridine), investigated by single-crystal X-ray diffraction, magnetization measurements, IR, UV/Vis and EPR (X-, Q-band and high-field) spectroscopies and density functional theory (DFT) calculations, are reported. Crystal structure of **1** (orthorhombic *Pcab* space group) consists of a square shaped macrocyclic $\{Cr_2(\mu\text{-}O)_4Nb_2\}$ core in which Cr^{III} and Nb^{V} ions are alternately bridged by oxo ions, and three uncoordinated water molecules. The intramolecular $Cr^{III}\cdots Cr^{III}$ distances through the $-O-Nb^{V}-O-$ bridges are 7.410(2) and 7.419(2) Å, while diagonal separation is 5.406(2) Å. The temperature dependence of magnetization, $M(T)$, evidences an antiferromagnetic ground state, which originates from a magnetic interaction between two Cr^{III} ions of spin 3/2 through two triatomic $-O-Nb^{V}-O-$ diamagnetic bridges. A spin Hamiltonian appropriate for polynuclear isolated magnetic units was used. The best fitting curve for this model is obtained with the parameters $g_{Cr} = 1.992(3)$, $J = -12.77(5)$ cm^{-1} and $|D| = 0.17(4)$ cm^{-1}. The $Cr^{III}\cdots Cr^{III}$ dimer model is confirmed by EPR spectra, which exhibit a pronounced change of their shape around the temperature corresponding to the intradimer coupling J. The EPR spectra simulations and DFT calculations reveal the presence of a single-ion anisotropy that is close to being uniaxial, $D = -0.31$ cm^{-1} and $E = 0.024$ cm^{-1}.

INTRODUCTION

During the last decades, heteropolynuclear metal complexes have been widely investigated not only for their ability to form different architectures and topologies, but also for their interest for applications in catalysis, photoluminescence, gas storage and separation, magnetism and multifunctional molecular materials.[1–4] Although the most often used elements for the preparation of these complexes are the 3d first row transition metals, many systems are also combining two or more different 3d and 4d metal ions.[5,6]

With the aim to control the magnetic properties of the heteropolynuclear complexes, L_t–M–L_b–M'–L_t (L_b = bridging ligand, L_t = terminal ligand), many strategies have been considered focusing on alternating the chemical nature of the metallic center (M and/or M') and bridging ligands (L_b) and their intramolecular arrangement (L_b–M and L_b–M' bond lengths and M–L_b–M' bond angles).[7,8] In particular, improving the delocalization between the magnetic centers could be reached by using long conjugated bridges, which lead to low energy $\pi \rightarrow \pi^*$ excitations as well as by small diamagnetic spin linkers such as Cl^-, O^{2-}, or closed-shell metal ions, which allow a direct M–M magnetic coupling. Thus, the main parameter enabling the control of such properties is the strength of the orbital overlap between the metal and ligand. Indeed, the presence of low-lying valence excitations results in large spin and charge polarization contributions, explaining the interest of using molecular ions such as oxalate, acetate, azide and conjugated bridges, for instance. New generations of strings of transition metal ions have been also proposed consisting to combine closed-shell metal ions with a spin carrier, which could be either an organic magnetic unit or a paramagnetic transition metal ion.[8–10]

In the search for suitable synthetic routes leading to novel and more diversified polynuclear species, we have introduced a new building block: the tris(oxalato)oxoniobate(V) anion, $[NbO(C_2O_4)_3]^{3-}$, to be used with different metal centers.[11–15] There are seven oxygen atoms coordinated to Nb^V in this anion, adopting a distorted pentagonal bipyramid geometry (Scheme 1). A special feature of this anion is that it can form heterometallic complexes through the bridging oxalate (μ-C_2O_4) and/or oxo (μ-O) group.[11,14–16]

Recent studies have shown intriguing chemistry in the family of the oxo-bridged heterometallic complexes. In particular, the occurrence of light-driven intramolecular metal-to-metal charge transfer (MMCT) enhances photochemical reactivity of these systems.[17,18] Moreover, this phenomenon can influence the magnetic properties, since light or heat stimulated charge transfer processes lead to a change of the spin-state of the metal center.[19,20] Such an unusual magnetic behavior, governed by MMCT, was already observed in structures based on –Cr–O–Cr– bridges, but the occurrence of this phenomenon is still hard to predict and the relationship between such light-induced electron transfer and molecular structure is not yet understood.[21]

As a result of our current investigation on this topic, a novel heterotetranuclear oxo-bridged compound $[Cr_2(bpy)_4(\mu\text{-}O)_4Nb_2(C_2O_4)_4]\cdot 3H_2O$ (**1**) (bpy = 2,2′-bipyridine) has been prepared and its structural, spectroscopic and magnetic properties have been investigated. Here we show that compound **1**, containing a square shaped $\{Cr_2(\mu\text{-}O)_4Nb_2\}$ core, exhibits relatively strong antiferromagnetic coupling between two chromium(III) ions mediated by two –O–Nb^V–O– diamagnetic bridges.

In many cases, the magnetic interaction in the polynuclear complexes, based on metal centers and bridging ligands, i.e. on the nature of the magnetic orbitals and the bridging geometry, can be predicted; in compound **1** any significant exchange coupling was not expected due to long intramolecular distances of ~7.4 Å between Cr^{III} centers bridged by diamagnetic atoms. Also, the magnetic coupling in compound **1** cannot be explained by a direct dipole-dipole magnetic interaction between the two Cr^{III} ions, which are too far apart (~5.4 Å). The SQUID and EPR measurements (X-, Q-band and high-field), combined with density functional theory (DFT) calculations have thus been carried out to identify without ambiguity the magnetic exchange path, and to explain the nature of magnetic interaction in compound **1**. Additionally, DFT calculations have clarified the absence of metal-to-metal charge transfer, which was considered as the other possibility for the interpretation of magnetic behavior of **1**, and finally confirmed antiferromagnetic behavior of two chromium(III) ions through diamagnetic bridges.

Exchange interactions between paramagnetic metal centers mediated by diamagnetic metal ion are known but are rare,[16,22–27] so the full comprehension of how the unpaired electrons of the metal centers feel each other through diamagnetic transition metal atom is still challenging.

EXPERIMENTAL SECTION

Materials and Physical Measurements. All chemicals were purchased from commercial sources and used without further purification. The starting compound $(NH_4)_3[NbO(C_2O_4)_3]\cdot H_2O$ was prepared following a specific procedure described previously.[11] Bis(bipyridine)chromium(III) precursor solution [$c(Cr^{III})$ = 0.04 M] was prepared in a CEM Discover Synthesis Unit microwave reactor, by refluxing an aqueous solution of $Cr(NO_3)_3\cdot 9H_2O$ and 2,2'-bipyridine in the molar ratio 1 : 2 for 15 minutes, under P = 150 W and T = 380 K.[28] Elemental analyses for C, H and N were performed with a Perkin–Elmer Model 2400 microanalytical analyser. The infrared spectra were recorded in the 4000–350 cm^{-1} region with samples as KBr pellets, with a Bruker Alpha FTIR spectrometer. Solid state electronic spectra were measured with a Shimadzu UV-VIS-NIR spectrophotometer (model UV-3600) equipped with an integrated sphere, using barium sulphate as reference.

Synthesis of $[Cr_2(bpy)_4(\mu\text{-}O)_4Nb_2(C_2O_4)_4]\cdot 3H_2O$ (1). An aqueous solution (10 mL) of $(NH_4)_3[NbO(C_2O_4)_3]\cdot H_2O$ (90.10 mg, 0.2 mmol) was added with a dropper to an aqueous solution (5 mL) containing chromium precursor complex [n(Cr) = 0.2 mmol; n(bpy) = 0.4 mmol]. The reaction mixture was stirred at room temperature for a short period of time. The dark orange polyhedral crystals of **1** appeared very quickly from the resulting clear red solution and the process of crystallization was completed within a period of two days. The crystals were separated from the solution by filtration, washed with water, and left to dry in air. The yield was 65.2%. Anal. calcd for $C_{48}H_{38}Cr_2N_8Nb_2O_{23}$: C, 41.64; H, 2.77; N, 8.09: Found: C, 41.45; H, 2.81; N, 8.11. IR data (KBr, cm^{-1}): 3527 (m), 3443 (m), 3119 (w), 3086 (w), 3039 (w), 1723 (s), 1708 (vs), 1677 (s), 1605 (m), 1567 (w), 1499 (w), 1474 (w), 1447 (m), 1364 (m), 1349 (s), 1317 (m), 1280 (sh), 1247 (w), 1210 (m), 1162 (w), 1100 (w), 1064 (w), 1048 (w), 1034 (w), 1023 (w), 923 (m), 860

(vs), 790 (m), 767 (m), 732 (m), 668 (w), 652 (w), 536 (m), 483 (w), 452 (w), 420 (w), 388 (w), 363 (w). UV/Vis data ($BaSO_4$, nm): 519, 450, 419, 393, 309, 261, 208.

Single-Crystal X-ray Study. The X-ray data of a single crystal of **1** were collected by ω-scans on an Oxford Diffraction Xcalibur Nova R diffractometer with mirror monochromated Cu-Kα radiation (λ = 1.54179 Å, microfocus tube, CCD detector) at room temperature [293(2) K] and also at lower temperature [93(2) K]. Measured intensity data were reduced using the CrysAlis[29] software package. The multi-scan absorption correction was applied. The crystal data, experimental conditions and final refinement parameters are summarized in Table 1. Molecular and crystal structures were solved by direct methods using the program SIR92,[30] and refined by the full-matrix least-squares method based on F^2 with anisotropic displacement parameters for all non-hydrogen atoms (SHELXL-97).[31] Both programs were operating under the WinGX[32] program package. Hydrogen atoms attached to the C atoms of the bipyridine ligands were treated as riding in idealized positions, with the C–H distances of 0.93 Å and displacement parameters assigned as $U_{iso}(H) = 1.2U_{eq}(C)$. All hydrogen atoms of the water molecules in **1** were recognized in the difference Fourier map. The O–H distances in those water molecules were restrained to a target value of 0.85(2) Å, and the H–O–H angle to 104°. Geometrical calculations were carried out with PLATON[33] and the figures were made by the use of the VESTA,[34] CCDC-Mercury[35] and ORTEP-III[32] programs.

Crystallographic data for this paper can be obtained free of charge via www.ccdc.cam.ac.uk/conts/retrieving.html (or from the Cambridge Crystallographic Data Centre, 12, Union Road, Cambridge CB2 1EZ, UK; fax: +44 1223 336033; or deposit@ccdc.cam.ac.uk). CCDC 1446578 contains the supplementary crystallographic data for this paper.

Table 1. Crystallographic Data and Structure Refinement Details for Compound $[Cr_2(bpy)_4(\mu\text{-}O)_4Nb_2(C_2O_4)_4]\cdot 3H_2O$ (1)

compound	**1**	
T (K)	293(2)	93(2)
crystal colour, habit	red, rhombohedra	orange, rhombohedra

empirical formula	$C_{48}H_{38}Cr_2N_8Nb_2O_{23}$	
fw (g mol^{-1})	1384.68	
crystal syst	orthorhombic	
space group	*Pcab*	
a (Å)	14.198(5)	14.042(5)
b (Å)	19.854(5)	19.640(5)
c (Å)	37.409(5)	37.320(5)
α (deg)	90	90
β (deg)	90	90
γ (deg)	90	90
V (Å^3)	10545(5)	10292(5)
Z	8	8
D_{calc} (g cm^{-3})	1.744	1.787
μ (mm^{-1})	7.580	7.766
F(*000*)	5568	5568
crystal size (mm^3)	0.25×0.12×0.05	0.26×0.08×0.04
Θ range (deg)	3.25–75.96	3.26–75.80
no. of measured reflections	36729	33845
no. of independent reflections	10883	10629
no. of observed reflections	9761	8773
no. of parameters, restraints	766, 9	772, 9
R_{int}	0.0327	0.0646
R, w*R* [I > 2σ(I)]	0.0427, 0.1127	0.0683, 0.1831
R, w*R* [all data]	0.0475, 0.1174	0.0791, 0.1935
goodness of fit, *S*	1.032	1.021
$\Delta\rho_{max}$, $\Delta\rho_{min}$ (e Å^{-3})	0.911, –1.041	1.022, –1.974

Magnetic Susceptibility and EPR Spectroscopy. The magnetization *M* of a powder sample of compound **1** was measured with an MPMS 5 commercial superconducting quantum interferometer device (SQUID) magnetometer. The measured magnetic moments of the sample were corrected by taking into account the sample holder and temperature-independent contributions of the core electrons in accordance

with the well-known Pascal constants. The temperature dependence of magnetization, $M(T)$, was measured under different magnetic fields, from 0.1 mT to 5 T, in the temperature range 2–330 K. Additionally, the field dependences of magnetization, $M(H)$, i.e. magnetic hysteresis loops, were measured at several stable temperatures in fields up to 5 T.

The electron paramagnetic resonance (EPR) measurements were performed in the low-frequency range 9.4–34.5 GHz and in the high-frequency range 97.6–326.4 GHz. In the former case resonator-based EPR spectrometers were used, including a custom-build spectrometer working in X-band (9.37 GHz) and a commercial Bruker Q-band (34.5 GHz) spectrometer. The magnetic field was varied between 0 and 1.2 T with an electromagnet. The high-frequency measurements were recorded on a custom-built transmission-type EPR spectrometer in the Faraday configuration with the microwave magnetic field being perpendicular to the static applied magnetic field provided by an Oxford superconducting magnet capable of reaching 17 T. In both types of spectrometers temperature was varied between room temperature and 5 K using continuous He-flow cryostats. In order to enhance the EPR signal-to-noise ratio the magnetic-field modulation technique was used and derivative EPR absorption spectra were therefore recorded. The same polycrystalline sample was used in all EPR experiments.

DFT Calculations. Two plane-wave self-consistent field (PWSCF) DFT codes have been used to theoretically describe the electronic and magnetic properties of the compound. More specifically the magnetic (collinear) ground state properties have been investigated using the QUANTUM ESPRESSO (QE) package[36] and the magnetic properties (magnetic exchange and anisotropy) using Vienna Ab-initio Simulation Package (VASP).[37,38] In both cases, the calculations were based on the density functional theory (DFT) using the Perdew-Burke-Ernzerhof (PBE)[39] functional under the Generalized Gradient Approximation (GGA), and Projector Augmented Wave (PAW)[40] functions have been used in the wave function basis set. It should be noticed that to have a proper description of the electron localization of the 3*d* states of Cr atoms, it is essential to go beyond standard DFT functionals. Here we have used two approaches, namely GGA+U[41] and HSE06[42] hybrid functionals. In GGA+U method, an effective Hubbard parameter of

$U_{\mathrm{eff}} = U - J = 3.5$ eV for the 3d(Cr) states has been used. The calculations have been done for one isolated molecule (90 K crystal structure / the surrounding water molecules are neglected) in a cubic supercell allowing to avoid interactions between the periodic images ($a = 20$ Å). For all investigations, the plane wave basis set is fixed by a cut-off energy of 500 eV and only the Γ-point is considered. The geometry optimization was carried out at the GGA+U level. Only ionic positions were relaxed and the optimization stopped when forces on each atom were smaller than 0.03 eV A^{-1}. Anisotropic magnetic properties were investigated by including spin-orbit coupling.

RESULTS AND DISCUSSION

Synthesis and Crystal Structure of 1. The neutral tetranuclear chromium(III)–niobium(V) complex of the formula $[Cr_2(bpy)_4(\mu\text{-}O)_4Nb_2(C_2O_4)_4]\cdot 3H_2O$ (**1**) is prepared using a very simple procedure at room temperature, from the reaction of aqueous solutions of tris(oxalato)oxoniobate(V) anions and bis(bipyridine)chromium(III) cations in the molar ratio 1 : 1 (Scheme 1). The obtained reddish crystals are moderately air-stable, not soluble in water and common organic solvents. Low solubility of **1** in all common solvents has unable further characterization of compound in solution (*i.e.* cyclic voltammetry).

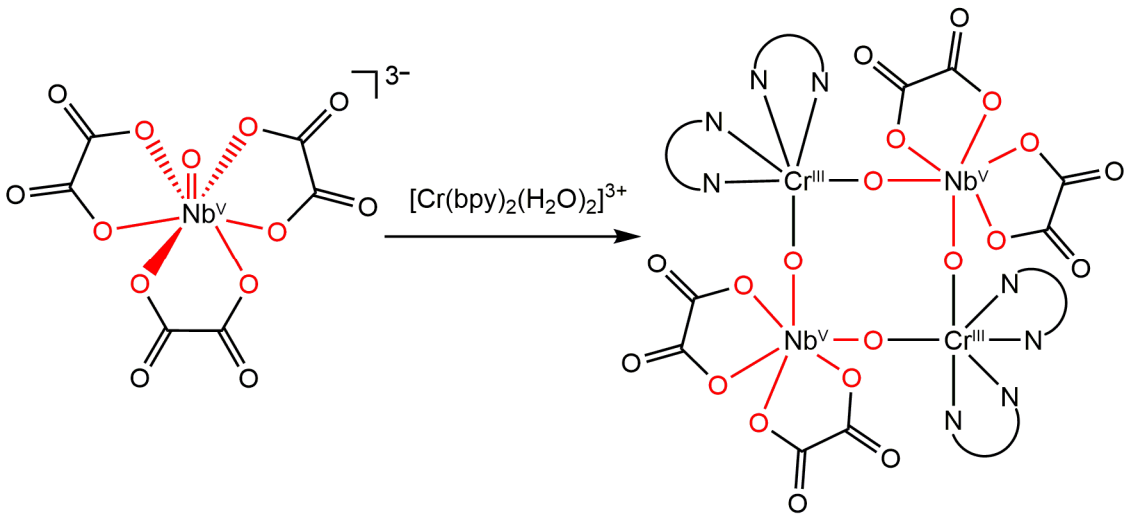

Scheme 1. The change in coordination sphere of Nb^V during the formation of compound **1**, from pentagonal bipyramid in $[NbO(C_2O_4)_3]^{3-}$ precursor to octahedron in $[Cr_2(bpy)_4(\mu\text{-}O)_4Nb_2(C_2O_4)_4]$ unit.

The titled compound crystallizes in the orthorhombic *Pcab* space group observed at 293 and 90 K (Table 1). Its crystal structure consists of a square shaped macrocyclic $\{Cr^{III}_2(\mu\text{-}O)_4Nb^{V}_2\}$ core, in which Cr^{III} and Nb^{V} ions are alternately bridged by oxo ions (Figures 1 and S1, Supporting Information), and three water molecules of crystallization. Ions Cr^{III} and Nb^{V} have an octahedral coordination, with each Cr^{III} ion surrounded by four N atoms from two bpy molecules and two bridging oxo atoms (Figures 1 and S1, Supporting Information). The Cr–N bond lengths (in average 2.059 Å; Tables S1 and S2 in the Supporting Information) are in good agreement with those found in other bis(bipyridine)chromium cations (in average 2.057 Å).[28]

Two chelating oxalate groups are coordinated to the Nb^{V} cation, as well as two bridging oxo atoms (Figures 1 and S1, Supporting Information). During the formation of compound **1**, the geometry of niobium coordination polyhedron is changed – from pentagonal bipyramid in $[NbO(C_2O_4)_3]^{3-}$ precursor to octahedron in $[NbO_2(C_2O_4)_2]^{3-}$ in **1** (Scheme 1). At 293 K, two Nb–$O_{oxalate}$ bonds located in the axial position, are found to be significantly shorter [2.029(4)–2.058(3) Å, in average 2.052 Å; Tables S3 and S4 in the Supporting Information] than the two Nb–$O_{oxalate}$ bonds located in the equatorial plane [2.152(3)–2.181(3) Å, in average 2.163 Å; Tables S3 and S4 in the Supporting Information]. In other structurally characterized bis(oxalato)niobate compounds, all Nb–$O_{oxalate}$ bonds are similar in length (average value of 2.118 Å).[6] It should be mentioned that after the DFT geometry optimization this difference is still observed but less pronounced, with 2.088 and 2.135 Å for axial and equatorial Nb–$O_{oxalate}$ average bond lengths, respectively (Tables S3 and S4, Supporting Information).

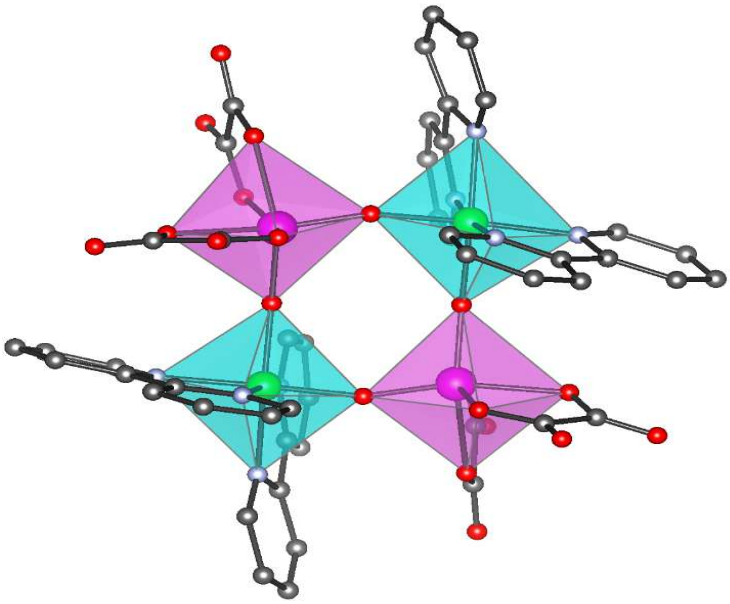

Figure 1. VESTA[33] drawing of the heterotetranuclear $[Cr_2(bpy)_4(\mu\text{-}O)_4Nb_2(C_2O_4)_4]$ unit in **1**, showing coordination polyhedra around metal centers. The octahedra around the Cr and Nb atoms are depicted in light blue and violet colors, respectively. Hydrogen atoms and solvent molecules are omitted for clarity.

In this compound, four (almost equal) Nb–O_{oxo} bonds (average: 1.799 Å, Tables S3 and S4, Supporting Information) are shorter than Cr–O_{oxo} bonds (with an average of 1.909 Å; Tables S1 and S2, Supporting Information), indicating that both oxygen atoms are coordinated to niobium(V) prior to formation of compound **1**. All known Nb=O bond lengths, contained in bis- and tris(oxalato)niobates found in the Cambridge Structural Database (CSD),[6] are shorter than 1.722(2) Å (in average 1.713 Å), showing that Nb–O bond character in **1** is closer to a single bond. Though designated as a double bond, similar bond length of Nb–O_{oxo} (in average 1.785 Å) was found in the only known compound containing $Cr^{III}_2Nb^{V}_2$ molecular square, $[Cr_2(dmso)_8(\mu\text{-}O)_4Nb_2(C_2O_4)_4]$,[16] but its crystal structure ($P\bar{1}$) differs significantly from the structure of **1** (*Pcab*). The Nb–$O_{oxalate}$ and Cr–O_{oxo} bond lengths in **1** are in good agreement with those observed in the mentioned compound (on average 2.113 Å and 1.908 Å, respectively).[16] Our DFT results confirm the present discussion with Nb–O_{oxo} bonds lengths of 1.87 Å, shorter than the Cr–O_{oxo} bonds (1.91 Å). As expected, all the optimized distances are slightly overestimated due to the use of the PBE-GGA functional in our calculations (Tables S1–S4, Supporting Information).

The average metal···metal distance across the oxo bridge is 3.673 Å (Table S5, Supporting Information). Two Cr^{III} atoms are diagonally separated by 5.406(2) Å (5.434 Å theoretically), and intramolecular $Cr^{III}\cdots Cr^{III}$ distances through the –O–Nb^{V}–O– bridges are 7.410(2) and 7.419(2) Å (close to 7.555 Å with DFT calculations).

Overall, the structure of the square motif, namely bond lengths, did not show significant changes as a function of temperature (Tables 1 and S1–S5, Supporting Information) ruling out the heat induced MMCT occurrence in this temperature range. At 293 K deviation from the planarity of the $\{Cr_2(\mu\text{-}O)_4Nb_2\}$ core [greatest is 0.231(3) Å for O4, Figure S1 in the Supporting Information] and values of the O–Nb–O [102.24(11) and 102.34(11)°, Tables S3 and S4 in the Supporting Information] as well as the Cr–O–Nb angles [range 158.53(16)–174.33(14)°, Table S5, Supporting Information] indicate a distorted square geometry. The molecular squares are quite well isolated from each other, with shortest distance between two molecules (centers of gravity of squares) being 10.030 Å. Separation of two atoms from these molecules is also the shortest and equals 8.294(1) Å [Cr2···Cr2].

Water molecules are involved in hydrogen bonds with uncoordinated oxygen atoms of oxalate ligands forming a three-dimensional (3D) supramolecular arrangement. Square units in **1** are additionally connected through aromatic stacking interactions along the *a* axis. Geometric parameters and graphical representation of hydrogen bonding and stacking interactions are given in the Supporting Information (Table S6 and S7, Figures S2 and S3).

IR and UV/Vis Spectroscopic Studies. The IR spectrum of compound **1** exhibits the absorption bands characteristic of chelating bidentate oxalate groups, bridging oxo atoms, and 2,2′-bipyridine ligands. The band of medium intensity found in the region 3670–3150 cm^{-1} originates from the O–H stretching vibration [ν(OH)] of water molecules. The spectrum shows several absorption bands ascribed to the vibrations of bidentate oxalate groups: ν_{as}(CO) at 1723, 1708 and 1677 cm^{-1}, ν_{s}(CO) at 1349 and 1210 cm^{-1}, δ(OCO) at 790 cm^{-1}.[14] The relatively broad absorption band in the region 930–770 cm^{-1} originates from vibrations of oxo bridges, with maximum at 860 cm^{-1} corresponding to the Cr–O–Nb asymmetric stretching vibration.[43]

Other absorption bands of significant intensity in the spectra correspond to different vibrations of coordinated 2,2′-bipyridine molecules.[43]

Solid state UV/Vis spectrum of compound **1** exhibits very similar pattern to other octahedral chromium(III) complexes with four N and two O donor atoms in the chromium coordination sphere (Figure S4 in the Supporting Information).[28] Chromium(III) ion (3*d*) in octahedral geometry shows three transitions: $^4T_{2g} \leftarrow {}^4A_{2g}$, $^4T_{1g}(F) \leftarrow {}^4A_{2g}$ and $^4T_{1g}(P) \leftarrow {}^4A_{2g}$. Latter transition usually occurs at the higher energy (UV) region, and is overlapped with more intense ligand transitions. Due to trigonal distortion of octahedral geometry around Cr^{III} in **1**, splitting of the $^4T_{2g}$ level in $^4A_1$ and ^4E, and the level $^4T_{1g}$, in $^4A_2$ and ^4E occurs, and four bands at 519, 450, 393 and 419 nm are recognized accordingly.[44] In the UV part of the spectrum stronger absorption bands are present corresponding to ligand-to-metal charge transfer (LMCT) transitions: N→Cr at 309 nm and O→Nb at 261 nm.[27,45,46]

For some Prussian-blue analogues of similar square shaped structure, absorption of 500–800 nm light was found to induce the intramolecular metal-to-metal charge transfer. This was accompanied by switch of non-magnetic ground state of compound to a magnetic state.[19,20] The same effect was observed in several transition metal oxo bridged compounds, but appearing under somewhat lower wavelenghths.[17,18,21] Even though compound **1** was a good candidate to expect the occurrence of MMCT phenomena, having both; the square shape core structure, and oxo bridges between transition metals (Cr^{III} and Nb^{V}), this type of transfer was not observed. Almost perfect overlap of UV/Vis spectra of **1** and the starting compounds (Figure S4), excludes the presence of additional absorption band, which could be assigned to MMCT.

Magnetization Study. Magnetization as a function of temperature $M(T)$ for compound **1** has been investigated for a broad range of static magnetic fields. Two series of measurement have been carried out, in ZFC (zero-field-cooled) and FC (field-cooled) regimes, always leading to an overlapping of the ZFC and FC curves, which is the signature of no freezing of magnetic moments in the system. In addition, we observe no sharp peak in the $M(T)$ for any field and almost the same shape of $M(T)/H$ for all measurements, which altogether evidences low-dimensional magnetic coupling in this compound. Similarly, the field dependences

of magnetization, $M(H)$, i.e. magnetic hysteresis loops are reversible at all measured temperatures down to 2 K, which also indicates the absence of long-range magnetic order. Moreover, they are linear above 7 K up to applied 5 T field, confirming additionally purity of the sample. Therefore, the temperature dependence of magnetization was analyzed using a spin Hamiltonian model appropriate for heteropolynuclear isolated magnetic units.

As shown in Figure 2, the magnetization tends to be zero in the 0-K limit, which indicates an antiferromagnetic singlet ground state and confirms that the sample is free of paramagnetic impurities. The observed antiferromagnetic ground state can be interpreted using two different models, the first one based on the interaction of two chromium(III) ions of spin 3/2, $Cr^{III}\cdots Cr^{III}$, through two diamagnetic bridges (Figure 1), and the second one based on metal-to-metal charge transfer from chromium to niobium atoms induced by temperature decrease,[17–20] making the square of four magnetic ions $Cr^{IV}\cdots Nb^{IV}\cdots Cr^{IV}\cdots Nb^{IV}\cdots$ with spins (1, 1/2, 1, 1/2), respectively, interacting ferromagnetically through the two oxo- and antiferromagnetically through the other two oxo-bridges. Both models allow fitting the measured magnetization data. However, our EPR and DFT results confirm the first model, involving only magnetic Cr^{III} ions.

The related spin Hamiltonian is thus given by

$$\boldsymbol{H} = -J\vec{S}_1 \cdot \vec{S}_2 + \mu_B(\vec{S}_1 + \vec{S}_2) \cdot \boldsymbol{g} \cdot \vec{B} + \vec{S}_1 \cdot \boldsymbol{D} \cdot \vec{S}_1 + \vec{S}_2 \cdot \boldsymbol{D} \cdot \vec{S}_2 \qquad (1)$$

where $\vec{S}_1$ and $\vec{S}_2$ are the spins of the two Cr^{III} magnetic sites within each dimer, J is the magnetic exchange interaction, μ_B the Bohr magneton, g the gyromagnetic factor of Cr^{III}, $\vec{B}$ the applied field, and $\boldsymbol{D}$ the single-ions anisotropy tensor, assumed as diagonal, where the transversal term in anisotropy was neglected (see EPR study). Alternative approach in modeling of magnetization is a giant-spin model, as was thoroughly studied previously.[47] However, here the Hamiltonian (1) was diagonalised directly, and without further approximations. The parameters of the calculated magnetization are fitted to the measured $M(T)$ above 4.5 K, using our own developed Python software (full matrix diagonalization without approximation of low field B or low exchange interaction J). The best fit of equation 1 to the experimental data (solid line in Figure 2)

was obtained with g_{Cr} = 1.992(3), J = –12.77(5) cm^{-1}, and |D| = 0.17(4) cm^{-1}. The normalized sum of squared deviations between data and model is:

$$R = \frac{\sum_i \left(M_i^{fit} - M_i^{exp}\right)^2}{\sum_i \left(M_i^{exp}\right)^2} = 5.8 \cdot 10^{-5}$$

(2)

The so-obtained J value is in good agreement with the recently published value of –12.0 cm^{-1} in a similar compound.[16]

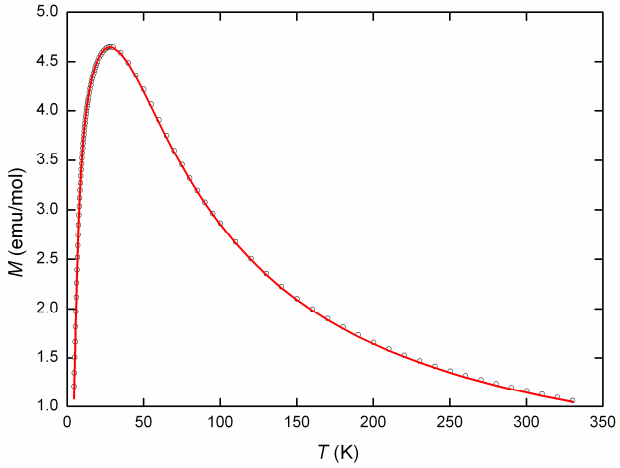

Figure 2. Temperature dependence of the magnetization for **1** measured in 0.01 T. The solid line represents the best fitted model curve.

It should be noted that introduction of the square spin tetramer model gives an even better fit with R = 4.8·10^{-6}. In this case, a very strong ferromagnetic exchange interaction (around 280 K) should couple neighbouring Cr^{IV} and Nb^{IV} ions, thus forming a (Nb–Cr) magnetic entity that carried an effective spin 3/2. The two (Nb–Cr) entities in the tetramer should then interact through a smaller antiferromagnetic exchange (around 39 K), leading again to the spin-singlet ground state. According to numerical M(T) simulations, measurements at higher temperatures, above 400 K, are needed in order to differentiate between the two models, but this is not possible due to the thermal decomposition of the compound. Moreover, the nonlinear low temperature M(H) dependences can also be accurately described using both models. EPR measurements

and DFT calculations have thus been performed extensively to determine the real mechanism of magnetic coupling within the system.

Although the systems with similar mechanisms of even stronger magnetic coupling of paramagnetic centers via the long bridges incorporating the diamagnetic metal ion are known,[16,22–27] our system, due to its interesting structural feature, has prompted us to consider two different models. Having in mind that proposed tetramer model can be possible if both metal centers are in oxidation state 4+, electron transfer (MMCT) from Cr^{III} (d^3) to Nb^{V} (d^0) should take place *a priori*. Since MMCT requires external stimuli such as light or heat to be exhibited, and no special electronic absorption in the spectrum either structural changes with temperature (93–293K) are noticed for compound **1**, the dimer model is more probable.[17–21]

EPR Study. Contrary to magnetization measurements, EPR allows the determination of the magnetic anisotropy terms in strongly exchange–coupled systems,[48] that are much smaller than the isotropic Heisenberg exchange interaction.[49–53] This technique is also able to provide a clear distinction between various possible magnetic anisotropy terms[50–52] and between different ionic valence states.[53]

The evolution of the EPR spectra of **1** with temperature and microwave frequency is shown in Figures 3 and 4. In contrast to isolated EPR centers whose EPR line shape is temperature independent and the intensity follows the Curie-law, the EPR signal is much more complex in our case. The EPR intensity, χ_{EPR}, which was determined by double-integration of the derivative EPR spectra and is proportional to the static susceptibility,[49,54] qualitatively follows the temperature dependence of the bulk susceptibility, χ_{bulk} (see *Magnetization study*), with a pronounced maximum around 30 K (Figure 3a). This corroborates the intrinsic nature of the EPR signal. Quantitative disagreements between χ_{EPR} and χ_{bulk} are due to the fact that part of the X-band EPR spectrum lies outside the experimental window (see below). Moreover, the line shape of the X-band spectra is atypical of isolated Cr^{III} ions and changes considerably between high and low temperatures. At high temperatures it consists of two peaks, one positioned around the expected *g*-factor value of 1.98[54] and the other at a much higher effective *g*-factor of 3.35. Increased resolution of the Q-band

spectrum reveals that the latter spectral component is more complex, as several high-"g-value" features are observed (Figure 3b).

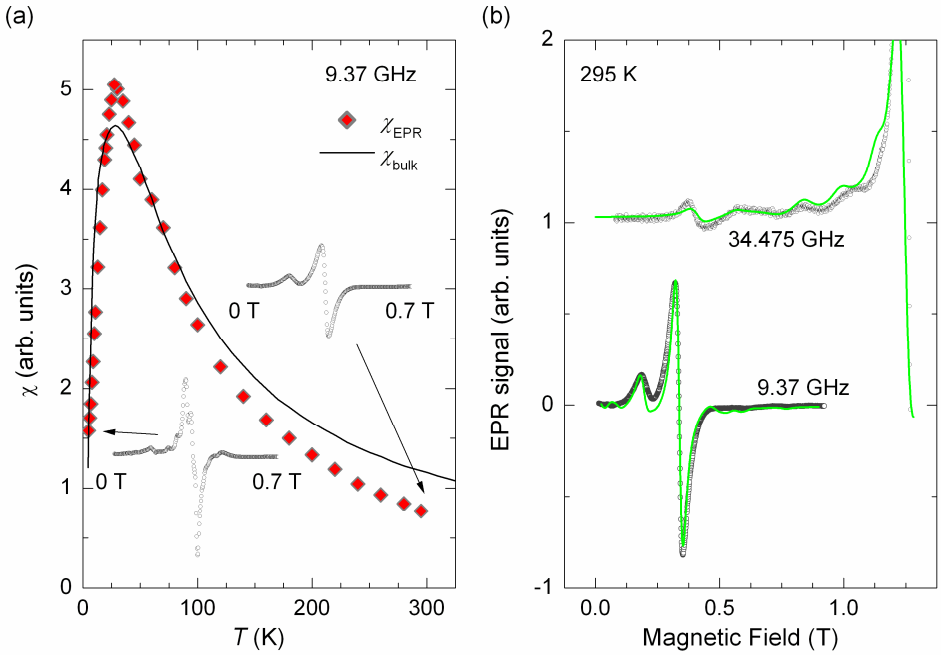

Figure 3. (a) The temperature dependence of the X-band (9.37 GHz) EPR susceptibility (intensity) compared to the bulk susceptibility. The corresponding high- and low-temperature spectra are displayed. (b) Comparison of the X- and Q-band EPR spectra at RT (grey symbols) and corresponding fits (green lines) of the $Cr^{III}\cdots Cr^{III}$ dimer model (see text for details).

A full, well-resolved EPR spectrum of the investigated compound could be recorded only in the high-frequency setup (Figure 4). The central line corresponding to the allowed $\Delta m = \pm 1$ transitions is split into several components and accompanied by the forbidden $\Delta m = \pm 2$ line, whose resonance field shifts twice slower with increasing frequency (Figure 4b). Similarly as in the X-band, the shape of the EPR spectrum changes considerably with temperature, with the line-shape crossover occurring around the temperature corresponding to the exchange coupling J of the dimer model (Figure 4a). Indeed, using the $Cr^{III}\cdots Cr^{III}$ dimer model, we can fit the EPR spectra at 104.00 GHz in the entire temperature range, with the Hamiltonian (3)

$$H = -J\vec{S}_1 \cdot \vec{S}_2 + \mu_B(\vec{S}_1 + \vec{S}_2) \cdot g \cdot \vec{B} + H_{SI} \quad (3)$$

The single-ion anisotropy of the form

$$H_{SI} = D\left[(S_1^z)^2 + (S_2^z)^2 - 2\frac{S(S+1)}{3}\right] + E\left[(S_1^x)^2 + (S_2^x)^2 - (S_1^y)^2 - (S_2^y)^2\right] \quad (4)$$

was used. The experimental spectra were simulated with the EasySpin software[55] by calculating the allowed dipolar transitions between all energy levels and powder averaging the results. Our best fit yields the two eigenvalues of the anisotropy tensor D = –0.31 cm^{-1} and E = 0.024 cm^{-1}, and the g-factor g = 1.98. The obtained g factor is slightly below the free-electron value, as usually found for the Cr^{III} ion.[54]

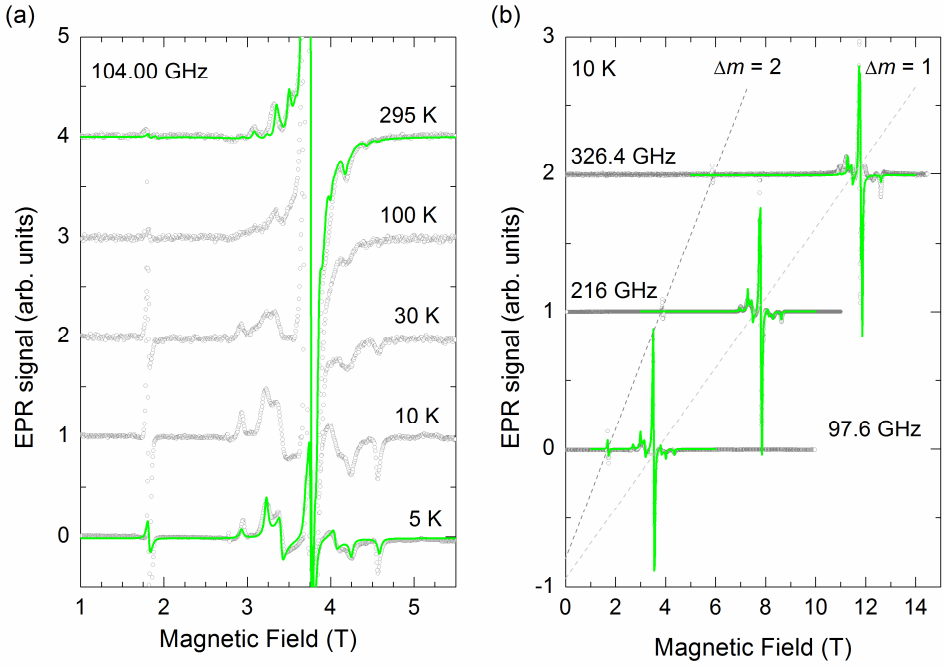

Figure 4. (a) The temperature dependence of the EPR spectra measured at 104.00 GHz and (b) the frequency dependence of the high-frequency EPR spectra at 10 K. The solid green lines are fits of the $Cr^{III}\cdots Cr^{III}$ dimer model (see text for details).

As the same set of parameters D, E corresponds well to high- and low-temperature spectra, the line-shape crossover around $T = J$ is obviously due to changing of population of different energy levels with temperature. The same parameters explain also the spectra at higher frequencies (Figure 4b), as well as the

multi-feature X-band and Q-band spectra (Figure 3b). The single-ion anisotropy in the investigated compound is close to being uniaxial. The derived magnitude of the anisotropy parameter D has a value, which is typical of a Cr^{III} ion in an octahedral oxygen environment.[54] Very similar magnitudes between 0.35–0.38 cm^{-1} were reported for Cr_2Zn_2 heterometallic complexes with distorted octahedral geometries and mixed O/N coordination,[56] similar as in compound **1**. In addition to the single-ion anisotropy, anisotropy of the form

$$D_{12}\left[S_1^z S_2^z - \frac{S(S+1)}{3}\right] \quad (5)$$

due to the dipolar interaction and the anisotropic exchange interaction within the $Cr^{III}\cdots Cr^{III}$ dimer is also expected. The dipolar contribution is exactly calculated :

$$D_{12}^{dip} = -\frac{3\frac{\mu_0}{4\pi}(g\mu_B)^2}{r^3} = -0.032\ \mathbf{cm^{-1}} \quad (6)$$

where μ_0 is the vacuum permeability and r = 5.41 Å is the $Cr^{III}\cdots Cr^{III}$ intradimer distance. Moreover, the symmetric anisotropic exchange is estimated as:

$$D_{12}^{ae} \sim \left(\frac{\Delta g}{g}\right)^2 J = 0.0014\ \mathbf{cm^{-1}} \quad (7)$$

Thus, the single-ion anisotropy D is far superior to D_{12} in the investigated compound.

Interestingly, we note that identical spectra can be simulated with a $Cr^{IV}\cdots Nb^{IV}\cdots Cr^{IV}\cdots Nb^{IV}\cdots$ spin-tetramer model. The obtained single-ion anisotropy of the Cr^{IV} ion in this model is somewhat larger than for the $Cr^{III}\cdots Cr^{III}$ dimer model, namely, D = –0.94 cm^{-1} and E = 0.07 cm^{-1}. However these values are incompatible with our DFT calculations (see below) and an order of magnitude larger single-ion anisotropy has been reported for this non-Kramers ion.[54] This makes the spin-tetramer model highly unlikely.

DFT Calculations. Figure 5a shows the total and partial densities of states determined using the hybrid functional HSE06 for a spin-polarized calculation, considering the magnetic moments of the two chromium sites in an antiferromagnetic (AFM) situation [the most stable magnetic order compared to the ferromagnetic

(FM) one]. The band gap appears to be mainly defined by the organic part of the system and is about 3.2 eV. The Cr(3*d*) and Nb(4*d*) states distribution leads to the conclusion that the oxidation states of these two elements in compound **1** are 3+ and 5+, respectively. In particular the Nb(4*d*) states are empty and centered at about 5 eV, well above the Fermi level. A small Nb(4*d*) contribution is observed in the valence band and is the signature of orbital overlap with the O(2*p*) states. Calculations have also been done using GGA+U formalism with various U_{eff} values for Cr atoms, the comparisons are presented in Table 2. The HSE06 magnetic moment (|2.86| μ_B/Cr) is well-reproduced for a Hubbard effective term U_{eff} equal to 3.5 eV (|2.87| μ_B/Cr). As expected no magnetic moment is observed on the Nb sites ($4d^0$ electronic configuration). The

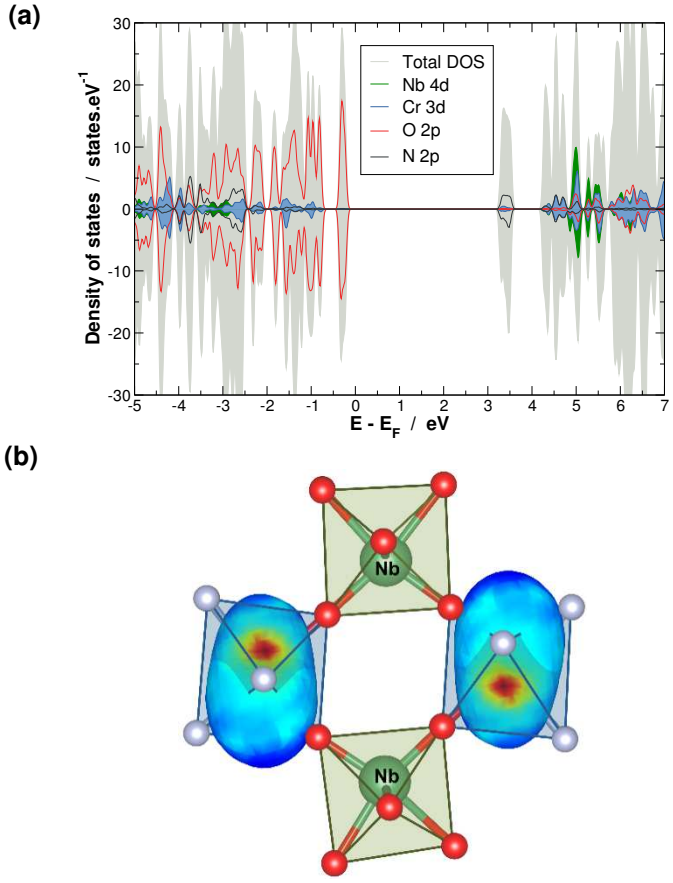

Figure 5. (a) Total DOS and projected PDOS onto specific atomic orbitals calculated in the HSE06 approximation. Carbon and hydrogen atoms are not represented for simplicity. (b) Representation of the local environment of the square shaped $\{Cr_2(\mu\text{-}O)_4Nb_2\}$ core. For each Cr^{III} ions the single-ion anisotropy is

represented. The easy and hard magnetization axes are emphasized in red and dark blue regions, respectively.

magnetic properties are thus related to the interaction between the two Cr magnetic moments, which can be described considering a super-superexchange (SSE) Cr–O···O–Cr path. To assess the related magnetic coupling, $J_{Cr\cdots Cr}$, a mapping analysis based on an Ising Hamiltonian has been considered.[57] Here, only two magnetic arrangements, FM and AFM, are needed to extract the $J_{Cr\cdots Cr}$ value, results for different U_{eff} values within GGA+U and using HSE06 hybrid functional given in Table 2. The AFM configuration is more stable than the FM. The following energy difference was used to estimate the superexchange parameter :

$$J_{Cr\cdots Cr} = 2/9(E_{AFM}–E_{FM}). \quad (8)$$

The U_{eff} value has a strong impact on $J_{Cr\cdots Cr}$, larger than the one observed for the magnetic moment. In particular the $J_{Cr\cdots Cr}$ value is twice larger with U_{eff} = 2.5 eV compared to the one with U_{eff} = 5.5 eV. Actually, increasing the U_{eff} term induces a contraction of Cr(3*d*) orbitals which leads to a reduction of the SSE coupling with the other magnetic centre. Experimentally the best fit for the dimer model leads to a $J_{Cr\cdots Cr}$ value of –12.5 cm^{-1}.

Table 2 Magnetic Moment of Cr Atoms and SSE Coupling Calculated by Varying U_{eff} Parameter in GGA+U and HSE06 Calculations

U_{eff}^{Cr} (eV)	2.5	3.5	4.5	5.5	HSE
μ_{Cr} (μ_B)	2.81	2.86	2.91	2.95	2.87
$J_{C\cdots Cr}$ (cm^{-1})	–25.0	–19.5	–16.0	–12.5	–10.4

It should be noted that we rejected the fitted experimental value of –19.5 cm^{-1} obtained for the tetramer model due to the absence of magnetic moment on Nb sites in our calculations. The absence of magnetic moment can also be evidenced looking at the magnetic dipole momentum distribution **M** in the square plane of compound **1** for FM and AFM configurations (Figure 6). Previously the

best comparison between GGA+U and HSE06 was obtained with U_{eff} = 3.5 eV, for the amplitude of μ_{Cr}. Interestingly, for the $J_{Cr\cdots Cr}$ value, GGA+U requires a larger U_{eff} value of 5.5 eV to reach the HSE06 value, with, respectively, –12.5 and –10.4 cm^{-1}. These two values are in very good agreement with the experimental estimation corresponding to the dimer model (–12.5 cm^{-1}). In HSE06 both Cr(3*d*) and O(2*p*) orbitals, which are involved in the SSE magnetic path, felt a contraction, which leads to decrease the magnetic coupling compared to a regular DFT calculation using a GGA functional. In contrast, only the Cr(3*d*) states felt a contraction in GGA+U. This is the reason why using «artificially» a larger U_{eff} value to compensate the fact that the O(2p) states are not involved in the GGA+U correction is necessary.

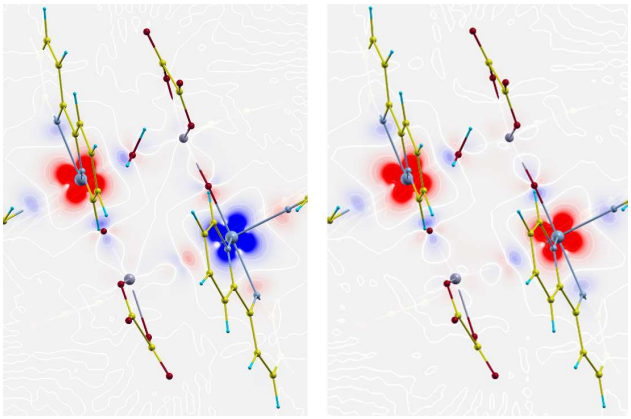

Figure 6. Magnetic dipole momentum distribution **M** in the square plane of **1**. The antiferromagnetic configuration is shown in left and ferromagnetic configuration in right panel.

Another way to confirm the validity of the dimer model is to estimate theoretically the single-ion anisotropy tensor. Experimentally, we obtained D = –0.31 cm^{-1} and E = 0.024 cm^{-1} for the dimer model and D = –0.94 cm^{-1} and E = 0.07 cm^{-1} for the tetramer model (see the EPR part). To estimate D and E parameters, DFT calculations including the spin-orbit coupling (DFT+SO) have been carried out. More specifically, the single-ion anisotropy (SIA) has been calculated using a similar strategy as the one of Weingart *et al.*[58] In this approach one Cr site is isolated by substituting the other Cr^{III} ion by a diamagnetic ion having the same oxidation state and very closed ionic radius, i.e. Ga^{3+} ion.

Figure 5b shows the single-ion anisotropy tensor shapes for the two Cr sites, with SIA = $E_{[uvw]} - E_{min}$, where $E_{[uvw]}$ is the energy deduced from spin–orbit calculations with the magnetization along the [uvw] crystallographic direction, and E_{min} the energy for the easy magnetization direction(s). From the knowledge of the single-ion anisotropy, the *D* and *E* parameters have been deduced based on an approach developed for the Magnetocrystalline Anisotropy Energy (MAE).[59,60] Both MAE and single-ion anisotropy are calculated by energy differences between different spin orientations, but the magnetization is induced by the overall of spins and an isolated spin respectively. The ground state energy $W(\theta,\phi)$ for a specific spin orientation depends directly on this orientation,

$$W(\theta,\phi) = W_Z + W'(\theta,\phi) = W_Z + DS\left(S-\frac{1}{2}\right)\left(cos^2\theta - \frac{1}{3}\right) + ES\left(S-\frac{1}{2}\right)\cos(2\phi)\,sin^2\theta \quad (9)$$

where θ and ϕ are the spherical angles, W_Z the Zeeman energy which is independent of the magnetic field direction. By performing a mapping analysis with energy calculations for specific spin orientations, we can easily extract the zero-field splitting parameters,

$$E = \frac{1}{2S\left(S-\frac{1}{2}\right)} \times \left(W(\theta=90,\phi=0) - W(\theta=90,\phi=90)\right) \quad (10)$$

$$D = \frac{1}{S\left(S-\frac{1}{2}\right)} \times \left(W(\theta=0,\phi=0) - \frac{1}{2}\left(W(\theta=90,\phi=0) + W(\theta=90,\phi=90)\right)\right) \quad (11)$$

For a given Cr site, the single-ion anisotropy can be expressed in a coordinate frame leading to a diagonal D matrix. In such a situation, we can define three magnetization axes with the following coordinates $(W_{easy}, \theta=0, \phi=0)$, $(W_{hard}, \theta=90, \phi=0)$ and $(W_{int}, \theta=90, \phi=90)$. *D* and *E* parameters can thus be expressed using:

$$E = \frac{1}{2S\left(S-\frac{1}{2}\right)} \times \left(W_{hard} - W_{int}\right) \quad (12)$$

$$D = \frac{1}{S\left(S-\frac{1}{2}\right)} \times \left(W_{easy} - \frac{1}{2}\left(W_{hard} + W_{int}\right)\right) \quad (13)$$

The resulting single-ion anisotropy parameters are $D = -0.29$ cm^{-1} and $E = 0.08$ cm^{-1} which clearly validates the dimer model (experimental values: $D = -0.31$ cm^{-1} and $E = 0.024$ cm^{-1}).

CONCLUSIONS

Very few structurally characterized oxo-bridged complexes are known, despite their relatively simple structure; so their synthesis is always a challenge. Even more interesting is that among structurally characterized systems only few include magnetic studies.

We have synthesized and characterized a new oxo-bridged compound $[Cr_2(bpy)_4(\mu\text{-}O)_4Nb_2(C_2O_4)_4]\cdot 3H_2O$ (**1**) and confirmed, experimentally and computationally, that triatomic bridge –O– Nb^V–O– is an effective mediator of the magnetic exchange interaction between chromium(III) ions.[16]

The tris(oxalato)oxoniobate(V) anion, $[NbO(C_2O_4)_3]^{3-}$ as a building block mostly forms heterometallic complexes through the bridging oxalate group, except in the reaction with chromium(III) precursor when oxo-bridged complexes are formed with six-coordinated Nb^V. Magnetic structure of **1** is based on a dimer model involving Cr^{III} sites with spin 3/2 interacting through –O–Nb^V–O– bridges. The antiferromagnetic super-exchange coupling $J = -12.77$ cm^{-1}, has been estimated from magnetization and EPR experiments and confirmed by DFT calculations. The EPR spectra verify the $Cr^{III}\cdots Cr^{III}$ model and provide evidence that this system exhibits single-ion anisotropy with $D = -0.31$ cm^{-1} and $E = 0.024$ cm^{-1}, thus being very close to uniaxial symmetry. These results are confirmed by DFT calculations including spin-orbit coupling which provide similar axial and rhombic ZFS parameters ($D = -0.29$ cm^{-1} and $E = 0.08$ cm^{-1}).

We have considered additional model for the interpretation of magnetic behavior of **1**, driven by light or heat induced intramolecular metal-to-metal charge transfer, resulting with change of metal oxidation states from $\{Cr^{III}–(\mu\text{-}O)–Nb^V\}$ to $\{Cr^{IV}–(\mu\text{-}O)–Nb^{IV}\}$. From the experimental solid state UV/Vis, which was supported with DFT calculations, the occurrence of light induced MMCT was not observed, since compared

to the spectra of starting compounds no additional absorption bands are recognized. Also, with lowering the temperature down to 100 K, the molecular structure of **1** stays unchanged, excluding the presence of thermally induced MMCT in this system.

ASSOCIATED CONTENT

Supporting Information. ORTEP-III drawing of molecule in **1** (Figure S1), geometric parameters of the chromium(III) and niobium(V) coordination spheres and describing core, as well as after DFT geometric optimizations (Tables S1–S5), hydrogen–bonding geometry and pattern (Table S6 and Figure S2), geometric parameters and pattern of the aromatic stacking interactions (Table S7 and Figure S3), solid state UV/Vis spectrum (Figure S4). X-ray crystallographic files (CIFs) for compound **1.** This material is available free of charge via the Internet at http://pubs.acs.org.

ACKNOWLEDGMENT

This work has been supported by the Croatian Science Foundation under the projects IP-2014-09-4079 and UIP-2014-09-8276. A.Z. acknowledges the financial support of the Slovenian Research Agency through the Program No. P1-0125 and the Project No. Bi-US/14-15-039. National High Magnetic Field Laboratory is supported by the NSF through the cooperative agreement DMR-1157490, the State of Florida and the Department of Energy. X.R. and W.L.D.H. thank CCIPL (Nantes) computing centre for computational facilities.

REFERENCES

(1) Kuppler, R. J.; Timmons, D. J.; Fang, Q.-R.; Li, J.-R.; Makal, T. A.; Young, M. D.; Yuan, D.; Zhao, D.; Zhuang, W.; Zhou, H.-C. Potential Applications of Metal-Organic Frameworks. *Coord. Chem. Rev.* **2009**, *253*, 3042–3066.

(2) Suh, M. P.; Cheon, Y. E.; Lee, E. Y. Syntheses and Functions of Porous Metallosupramolecular Networks. *Coord. Chem. Rev.* 2008, *252*, 1007–1026.

(3) Yamada, T.; Otsubo, K.; Makiura, R.; Kitagawa, H. Designer Coordination Polymers: Dimensional Crossover Architectures and Proton Conduction. *Chem. Soc. Rev.* **2013**, *42*, 6655–6669.

(4) Biswas, S.; Naiya, S.; Gómez-García, C. J.; Ghosh, A. Synthesis of the First Heterometalic Star-Shaped Oxido-Bridged $MnCu_3$ Complex and its Conversion into Trinuclear Species Modulated by Pseudohalides (N_3^-,NCS^- and NCO^-): Structural Analyses and Magnetic Properties. *Dalton Trans.* **2012**, *41*, 462–473.

(5) Murrie, M. Cobalt(II) Single-Molecule Magnets. *Chem. Soc. Rev.* **2010**, *39*, 1986–1995.

(6) Groom, C. R.; Bruno, I. J.; Lightfoot, M. P.; Ward, S. C. The Cambridge Structural Database. *Acta Crystallogr.* **2016**, *B72*, 171–179.

(7) Weihe, H.; Güdel, H. Angular and Distance Dependence of the Magnetic Properties of Oxo-Bridged Iron(III) dimers. *J. Am. Chem. Soc.* **1997**, *119*, 6539–6543.

(8) Malrieu, J. P.; Caballol, R.; Calzado, C. J.; de Graaf, C.; Guihéry, N. Magnetic Interactions in Molecules and Highly Correlated Materials: Physical Content, Analytical Derivation, and Rigorous Extraction of Magnetic Hamiltonians. *Chem. Rev.* **2014**, *114*, 429–492.

(9) Rohmer, M.-M.; Liu, I. P.-C.; Lin, J.-C.; Chiu, M.-J.; Lee, C.-H.; Lee, G.-H.; Bénard, M.; López, X.; Peng, S.-M. Structural, Magnetic, and Theoretical Characterization of a Heterometallic Polypyridylamide Complex. *Angew. Chem. Int. Ed.* **2007**, *46*, 3533–3536.

(10) Bénard, M.; Berry, J. F.; Cotton, F. A.; Gaudin, C.; López, X.; Murillo, C. A.; Rohmer, M.-M. Structure and Magnetism of $[M_3]^{6/7+}$ Metal Chain Complexes from Density Functional Theory: Analysis for Copper and Predictions for Silver. *Inorg. Chem.* **2006**, *45*, 3932–3940.

(11) Jurić, M.; Popović, J.; Šantić, A.; Molčanov, K.; Brničević, N.; Planinić, P. Single-Step Preparation of the Mixed Ba^{II}–Nb^{V} Oxides from a Heteropolynuclear Oxalate Complex. *Inorg. Chem.* **2013**, *52*, 1832–1842.

(12) Jurić, M.; Perić, B.; Brničević, N.; Planinić, P.; Pajić, D.; Zadro, K.; Giester, G.; Kaitner, B. Supramolecular Motifs and Solvatomorphism within the Compounds $[M(bpy)_3]_2[NbO(C_2O_4)_3]Cl\cdot nH_2O$(M = Fe^{2+}, Co^{2+}, Ni^{2+}, Cu^{2+} and Zn^{2+}; n = 11, 12). Syntheses, Structures and Magnetic Properties. *Dalton Trans.* **2008**, 742–754.

(13) Šestan, M.; Perić, B.; Giester, G.; Planinić, P.; Brničević, N. Another Structure Type of Oxotris(oxalato)niobate(V): Molecular and Crystal Structure of $Rb_3[NbO(C_2O_4)_3]\cdot 2H_2O$. *Struct. Chem.* **2005**, *16*, 409–414.

(14) Jurić, M.; Perić, B.; Brničević, N.; Planinić, P.; Pajić, D.; Zadro, K.; Giester, G. Structure, Stacking Interactions and Magnetism of Compounds with Oxalate-Bridged Dinuclear $Cu^{II}Cu^{II}$ and $Cu^{II}Nb^{V}$ Units. *Polyhedron* **2007**, *26*, 659–672.

(15) Jurić, M.; Planinić, P.; Brničević, N.; Matković-Čalogović, D. Synthesis, Properties and Crystal Structure of a Zn,Nb Compound with Homo- and Heterodinuclear Oxalate-Bridged Units – $[\{Zn(bpy)_2\}_2(\mu\text{-}C_2O_4)][Zn(bpy)_2(\mu\text{-}C_2O_4)NbO(C_2O_4)_2]_2\cdot 0.5bpy\cdot 7H_2O$: The Impact of Weak Interactions on the Crystal Packing. *J. Mol. Struct.* **2008**, *888*, 266–276.

(16) Oliveira, W. X. C.; Pereira, C. L. M.; Pinheiro, C. B.; Cano, J.; Lloret, F.; Julve, M. Relatively Strong Intramolecular Antiferromagnetic Coupling in a Neutral $Cr^{III}_2Nb^{V}_2$ Heterobimetallic Molecular Square. *Chem. Commun.* **2015**, *51*, 11806–11809.

(17) Wu, X.; Huang, T.; Lekich, T. T.; Sommer, R. D.; Weare, W. W. Synthesis of Unsupported d^1–d^x Oxido-Bridged Heterobimetallic Complexes Containing V^{IV}: A New Direction for Metal-to-Metal Charge Transfer. *Inorg. Chem.* **2015**, *54*, 5322–5328.

(18) Falzone, A. J.; Nguyen, J.; Weare, W. W.; Sommera, R. D.; Boyle, P. D. An Unsupported Metal Hydroxide for the Design of Molecular μ-Oxo Bridged Heterobimetallic Complexes. *Chem. Commun.* **2014**, *50*, 2139–2141.

(19) Zhang, Y.-Z.; Ferko, P.; Siretanu, D.; Ababei, R.; Rath, N. P.; Shaw, M. J.; Clérac, R.; Mathonière, C.; Holmes, S. M. Thermochromic and Photoresponsive Cyanometalate Fe/Co Squares: Toward Control of the Electron Transfer Temperature. *J. Am. Chem. Soc.* **2014**, *136*, 16854−16864;

(20) Nihei, M.; Sekine, Y.; Suganami, N.; Nakazawa, K.; Nakao, A.; Nakao, H.; Murakami, Y.; Oshio. H. Controlled Intramolecular Electron Transfers in Cyanide-Bridged Molecular Squares by Chemical Modifications and External Stimuli. *J. Am. Chem. Soc*. **2011**, *133*, 3592–3600.

(21) Morsing, T. J.; Bendix, J.; Weihe, H.; Døssing, A. Oxo-Bridged Dinuclear Chromium(III) Complexes: Correlation between the Optical and Magnetic Properties and the Basicity of the Oxo Bridge. *Inorg. Chem*. **2014**, *53*, 2996−3003.

(22) Journaux, Y.; Sletten, J.; Kahn, O. Interactions in $Cu^{II}Cu^{II}Cu^{II}$, $Cu^{II}Zn^{II}Cu^{II}$, and $Cu^{II}Ni^{II}Cu^{II}$ Trinuclear Species. Crystal Structure of Bis(N,N'-bis(3-aminopropyl)oxamido)tricopper(II) Perchlorate. *Inorg. Chem.* **1986**, *25*, 439–447.

(23) Chaudhuri, P.; Winter, M.; Wieghardt, K.; Gehring, S.; Haase, W.; Nuber, B.; Weiss, J. Syntheses and Magnetic Properties of a Heteropolyoxotungsten(VI)iron(III) Cation and $[LFe^{III}(\mu\text{-}MO_4)_3Fe^{III}L]$ Complexes (M = Chromium(VI), Molybdenum(VI)). Crystal Structures of $L_2Fe_2(CrO_4)_3\cdot H_2O$ and $[L_3Fe_3W_4O_{14}(OCH_3)_3](ClO_4)_2\cdot 0.5H_2O$ (L = 1,4,7-Trimethyl-1,4,7-triazacyclononane). *Inorg. Chem.* **1988**, 27, 1564–1569.

(24) Chaudhuri, P.; Winter, M.; Della Védova, B. P. C.; Bill, E.; Trautwein, A.; Gehring, S.; Fleischhauer, P.; Nuber, B.; Weiss, J. Syntheses, Redox Behavior, and Magnetic and Spectroscopic Properties of $Cu^{II}Cu^{II}Cu^{II}$, $Cu^{II}Ni^{II}Cu^{II}$, and $Cu^{II}Pd^{II}Cu^{II}$ Species. Crystal Structure of $[L_2Cu_2Cu(dmg)_2Br]ClO_4\cdot CH_3OH$ (L = 1,4,7-Trimethyl-1,4,7-triazacyclononane; dmg = Dimethylglyoximato(2-)). *Inorg. Chem.* **1991**, *30*, 2148–2157.

(25) Oshio, H.; Kikuchi, T.; Ito, T. A Ferromagnetic Interaction between Cu^{2+} Centers through a $[CrO_4]^{2-}$ Bridge: Crystal Structures and Magnetic Properties of $[\{Cu(acpa)\}_2(\mu\text{-}MO_4)]$ (M = Cr, Mo) (Hacpa = *N*-(1-Acetyl-2-propyridene)(2-pyridylmethyl)amine). *Inorg. Chem.* **1996**, *35*, 4938–4941.

(26) Ruiz, R.; Julve, M.; Faus, J.; Lloret, F.; Carmen Muñoz, M.;Journaux, Y.; Bois, C. Ferromagnetic Coupling between Copper(II) Centers through the Diamagnetic Zinc(II) Ion: Crystal Structure and Magnetic Properties of $[Cu_2Zn(Hdmg)_2(dmg)_2(H_2O)]\cdot 0.5H_2dmg\cdot H_2O$ (H_2dmg = Dimethylglyoxime). *Inorg. Chem.* **1997**, *36*, 3434-3439.

(27) Buvaylo, E. A.; V. N. Kokozay, Vassilyeva, O. Yu.; Skelton, B. W.; Jezierska, J.; Brunel, L. C.; Ozarowski, A. A Cu–Zn–Cu–Zn Heterometallomacrocycle Shows Significant Antiferromagnetic Coupling between Paramagnetic Centre*s* Mediated by Diamagnetic Metal. *Chem. Commun*. **2005**, 4976–4978.

(28) Androš, L.; Jurić, M.; Molčanov, K.; Planinić, P. Supramolecular Architectures of Novel Chromium(III) Oxalate Complexes: Steric Effects of the Ligand Size and Building-Blocks Approach. *Dalton Trans.* **2012**, *41*, 14611–14624.

(29) Agilent, *CrysAlis PRO*. Agilent Technologies Ltd, Yarnton, Oxfordshire, England, 2014.

(30) Altomare, A.; Cascarano, G.; Giacovazzo, C.; Guagliardi, A.; Burla, M. C.; Polidori, G.; Camalli, M. *SIR*92 - A Program for Automatic Solution of Crystal Structures by Direct Methods. *J. Appl. Crystallogr.* **1994**, *27*, 435.

(31) Sheldrick, G. M. Crystal Structure Refinement with *SHELXL*. *Acta Crystallogr.* **2015***, C71*, 3−8.

(32) Farrugia, L. J. *WinGX* and *ORTEP for Windows*: An Update . *J. Appl. Crystallogr.* **2012**, *45*, 849−854.

(33) Spek, A. L. Structure Validation in Chemical Crystallography. *Acta Crystallogr.* **2009**, *D65*, 148–155.

(34) Momma, K.; Izumi, F. *VESTA 3* for Three-Dimensional Visualization of Crystal, Volumetric and Morphology Data. *J. Appl. Crystallogr.* **2011**, *44*, 1272–1276.

(35) Macrae, F.; Edgington, P. R.; McCabe, P.; Pidcock, E.; Shields, G. P.; Taylor, R.; Towler, M.; van de Streek, J. *Mercury*: Visualization and Analysis of Crystal Structures. *J. Appl. Crystallogr.* **2006**, *39*, 453–457.

(36) Giannozzi, P.; Baroni, S.; Bonini, N.; Calandra, M.; Car, R.; Cavazzoni, C.; Ceresoli, D.; Chiarotti, G. L.; Cococcioni, M.; Dabo, I.; Dal Corso, A.; de Gironcoli, S.; Fabris, S.; Fratesi, G.; Gebauer, R.; Gerstmann, U.; Gougoussis, C.; Kokalj, A.; Lazzeri, M.; Martin-Samos, L.; Marzari, N.; Mauri, F.; Mazzarello, R.; Paolini, S.; Pasquarello, A.; Paulatto, L.; Sbraccia, C.; Scandolo, S.; Sclauzero, G.; Seitsonen, A. P.; Smogunov, A.; Umari, P.; Wentzcovitch, R. M. QUANTUM ESPRESSO: A Modular and Open-Source Software Project for Quantum Simulations of Materials. J. Phys.: Conden. Matter. 2009, 21, 395502.

(37) Kresse, G.; Hafner, J. *Ab Initio* Molecular Dynamics for Liquid Metals. *Phys. Rev. B* **1993**, *47*, 558–561.

(38) Kresse, G.; Furthmüller, J. Efficient Iterative Schemes for *Ab Initio* Total-Energy Calculations Using a Plane-Wave Basis Set. *Phys. Rev. B* **1996**, *54*, 11169–11186.

(39) Perdew, J. P.; Burke, K.; Ernzerhof, M. Generalized Gradient Approximation Made Simple. Phys. Rev. Lett. 1996, 77, 3865–3868.

(40) Kresse, G.; Joubert, D. From Ultrasoft Pseudopotentials to the Projector Augmented-Wave Method. *Phys. Rev. B* **1999**, *59*, 1758–1775.

(41) Dudarev S. L.; Botton G. A.; Savrasov S. Y.; Humphreys C. J.; Sutton A. P. Electron-Energy-Loss Spectra and the Structural Stability of Nickel Oxide: An LSDA+U Study. *Phys. Rev. B* **1998**, *57*, 1505–1509.

(42) Krukau, A. V.; Vydrov, O. A.; Izmaylov, A. F.; Scuseria, G. E. Influence of the Exchange Screening Parameter on the Performance of Screened Hybrid Functionals. *J. Chem. Phys*. **2006**, *125*, 224106.

(43) Nakamoto, K. *Infrared and Raman Spectra of Inorganic and Coordination Compounds*, 6th ed.; John Wiley: New York, 2009.

(44) Landron, S.; Lepetit, M.-B. Importance of t_{2g}–e_g Hybridization in Transition Metal Oxides**.** *Phys. Rev. B* **2008**, *77*, 125106.

(45) McDaniel, A. M.; Tseng, H.-W.; Damrauer, N. H.; Shores, M. P. Synthesis and Solution Phase Characterization of Strongly Photooxidizing Heteroleptic Cr(III) Tris-Dipyridyl Complexes. *Inorg. Chem.* **2010**, *49*, 7981–7991.

(46) Goforth, S. K.; Gill, T. W.; Weisbruch, A. E.; Kane-Maguire, K. A.; Helsel, M. E.; Sun, K. W.; Rodgers, H. D.; Stanley, F. E.; Goudy, S. R.; Wheeler, S. K.; Wheeler, J. F.; Kane-Maguire, N. A. P.

Synthesis of *cis*-[Cr(diimine)$_2$(1-methylimidazole)$_2$]$^{3+}$ Complexes and an Investigation of Their Interaction with Mononucleotides and Polynucleotides. *Inorg. Chem.* **2016**, *55*, 1516−1526.

(47) Morsing, T. J.; Weihe, H.; Bendix, J. Probing Effective Hamiltonian Operators by Single-Crystal EPR: A Case Study Using Dinuclear Cr(III) Complexes. *Inorg. Chem.* **2016**, *55*, 1453–1460.

(48) Bencini, A.; Gatteschi, D. *Electron Paramagnetic Resonancen of Exchange Coupled Systems*; Springer: Berlin, 1990.

(49) Zorko, A.; Nellutla, S.; van Tol, J.; Brunel, L. C.; Bert, F.; Duc, F.; Trombe, J.-C.; de Vries, M. A.; Harrison, A.; Mendels, P. Dzyaloshinsky-Moriya Anisotropy in the Spin-1/2 Kagome Compound $ZnCu_3(OH)_6Cl_2$. *Phys. Rev. Lett.* **2008**, *101*, 026405.

(50) Herak, M.; Zorko, A.; Arčon, D.; Potočnik, A.; Klanjšek, M.; van Tol, J.; Ozarowski, A.; Berger, H. Symmetric and Antisymmetric Exchange Anisotropies in Quasi-One-Dimensional $CuSe_2O_5$ as Revealed by ESR. *Phys. Rev. B* **2011**, *84*, 184436.

(51) Zorko, A.; Pregelj, M.; Potočnik, A.; van Tol, J.; Ozarowski, A.; Simonet, V.; Lejay, P.; Petit, S.; Ballou, R. Role of Antisymmetric Exchange in Selecting Magnetic Chirality in $Ba_3NbFe_3Si_2O_{14}$. *Phys. Rev. Lett.* **2011**, *107*, 257203.

(52) Zorko, A.; Bert, F.; Ozarowski, A.; van Tol, J.; Boldrin, D.; Wills, A. S.; Mendels, P. Dzyaloshinsky-Moriya Interaction in Vesignieite: A Route to Freezing in a Quantum Kagome Antiferromagnet. *Phys. Rev. B* **2013**, *88*, 144419.

(53) Zorko, A.; Pregelj, M.; Luetkens, H.; Axelsson, A.-K.; Valant, M. Intrinsic Paramagnetism and Aggregation of Manganese Dopants in $SrTiO_3$. *Phys. Rev. B* **2014**, *89*, 094418.

(54) Abragam, A.; Bleaney, B. *Electron Paramagnetic Resonance of Transition Ions*; Oxford University Press: Oxford, 1970.

(55) Stoll, S.; Schweiger, A. EasySpin, a Comprehensive Software Package for Spectral Simulation and Analysis in EPR. *J. Magn. Reson.* **2006**, *178*, 42–55.

(56) Semenaka, V. V.; Nesterova, O. V.; Kokozay, V. N.; Dyakonenko, V. V.; Zubatyuk, R. I.; Shishkin, O. V.; Boča, R.; Jezierska, J.; Ozarowski, A. Cr^{III}–Cr^{III} Interactions in Two Alkoxo-Bridged Heterometallic Zn_2Cr_2 Complexes Self-Assembled from Zinc Oxide, Reinecke's Salt, and Diethanolamine. *Inorg. Chem.* **2010**, *49*, 5460–5471.

(57) Xiang, H.; Lee, C.; Koo, H.-J.; Gonga, X.; Whangbo, M.-H. Magnetic Properties and energy-Mapping Analysis. *Dalton Trans.* **2013**, *42*, 823–853.

(58) Weingart, C.; Spaldin, N.; Bousquet, E. Noncollinear Magnetism and Single-Ion Anisotropy in Multiferroic Perovskites. *Phys. Rev. B* **2012**, *86*, 094413.

(59) Pederson, M. R.; Khanna, S. N. Magnetic Anisotropy Barrier for Spin Tunneling in $Mn_{12}O_{12}$ molecules. *Phys. Rev. B* **1999**, *60*, 9566.

(60) van Wullen, C. Magnetic anisotropy from density functional calculations. Comparison of Different Approaches: $Mn_{12}O_{12}$ Acetate as a Test Case. *J. Chem. Phys*. **2009**, *130*, 194109.

TABLE OF CONTENTS SYNOPSIS

A new heterotetranuclear compound $[Cr_2(bpy)_4(\mu\text{-}O)_4Nb_2(C_2O_4)_4]\cdot 3H_2O$ exhibits an antiferromagnetic ground state, coming from two Cr^{III} ions interacting through two –O–Nb^{V}–O– diamagnetic bridges, as revealed from magnetization modeling and confirmed by EPR spectra and DFT calculations.